Microporous and Mesoporous Materials 345 (2022) 112280

Contents lists available at ScienceDirect

Microporous and Mesoporous Materials

journal homepage: www.elsevier.com/locate/micromeso

Highly-efficient removal of Pb (II) from water by mesoporous amino functionalized silica aerogels: Experimental, DFT investigations and Life Cycle Assessment

Yaoyao Zhang [a,b,c], Luca Magagnin [c,**], Kangze Yuan [d,***], Zhengwen Wei [a,b], Xishe Wu [b], Zhenyi Jiang [e], Wei Wang [a,b,*]

[a] Key Laboratory of Subsurface Hydrology and Ecological Effects in Arid Region of the Ministry of Education, Chang'an University, Xi'an, Shaanxi, 710054, PR China
[b] School of Water and Environment, Chang'an University, Xi'an, Shaanxi, 710054, PR China
[c] Department of Chemistry, Materials and Chemical Engineering "Giulio Natta", Politecnico di Milano, via Mancinelli 7, 20131, Milano, Italy
[d] College of Geological Engineering and Geomatics, Chang'an University, Xi'an, Shaanxi, 710054, PR China
[e] Institute of Modern Physics, Northwest University, Xi'an, Shaanxi, 710054, PR China

ARTICLE INFO

Keywords:
Amino-functionalized
Adsorption
Pb (II)
Mechanism
DFT
LCA

ABSTRACT

Mesoporous amino functionalized silica aerogels (MASA-X) with high adsorption capacity were prepared at ambient pressure conditions for removal of Pb (II) ions from water. Supported by SEM images and FTIR spectra, the presence of $-NH_2$ groups and porous structures on the surface of MASA-X were demonstrated, which played a critical role in promoting the interfacial adsorption process. The adsorption isotherm fitted well by Langmuir model, indicating that the adsorption occurred on a homogeneous surface and the maximum adsorption capacity of MASA-1, MASA-2, MASA-3, MASA-4 were 444.4 mg/g, 628.93 mg/g, 549.45 mg/g and 286.53 mg/g, respectively, and MASA-2 demonstrated optimal adsorption performance. The kinetic data showed good correlation coefficient with the pseudo-second order kinetic model, and the adsorption equilibrium of MASA-1, MASA-2, MASA-3, MASA-4 were reached in 120 min, 60 min, 20 min and 20 min, respectively. And raising temperature facilitated the adsorption of Pb (II) as it was a spontaneous and endothermic process. It was noteworthy that MASA-2 showed satisfactory reusability after eight adsorption-desorption cycles. FTIR, XPS coupled with Density Functional Theory (DFT) calculation revealed that the involvement of monodentate N atoms in the coordination with Pb (II) on adsorption of Pb (II) by MASA-2. The environmental impact of the MASA-2 preparation process was calculated through Life Cycle Assessment (LCA) and by analyzing the contribution of each material in the production of MASA-2, a more environmentally friendly and effective production strategy has been finally proposed, which could facilitate the promotion of MASA-X adsorbents in the heavy metal contaminated water market.

1. Introduction

Water pollution has become a global problem, especially heavy metal pollution has been widely concerned because of its non-biodegradability and easy bioaccumulation [1,2]. Lead (Pb) is one of the most toxic heavy metals, if it enters the human body through the food chain, it will cause serious harm such as neurobehavioral disorder and renal function damage [3]. Therefore, the removal of Pb (II) from water has been studied extensively. Among various remediation technologies such as chemical precipitation [4], ion exchange [5], membrane filtration [6], absorption [7] and electrochemical treatment [8], adsorption is considered to be an effective and attractive method due to its low cost, high efficiency and environmental friendliness [9,10].

Various materials such as activated carbon [11], molecular sieves [12], clays [13], carbon nanotubes [14], chitosan [15], silica aerogels [16] and many other materials [17–19] have been reported as

* Corresponding author. Key Laboratory of Subsurface Hydrology and Ecological Effects in Arid Region of the Ministry of Education, Chang'an University, Xi'an, Shaanxi, 710054, PR China.
** Corresponding author.
*** Corresponding author.
E-mail addresses: luca.magagnin@polimi.it (L. Magagnin), 2018026021@chd.edu.cn (K. Yuan), wwchem@chd.edu.cn (W. Wang).

https://doi.org/10.1016/j.micromeso.2022.112280
Received 8 August 2022; Received in revised form 7 October 2022; Accepted 11 October 2022
Available online 14 October 2022

adsorbents for the removal of heavy metal ions from solutions. Compared with other adsorbents, silica aerogels have the advantage of high specific surface area, high porosity, lightweight structure, and easy surface functionalization [20]. Conventional silica aerogels were typically dried by supercritical drying process, considering cost and safety issues, producing them under ambient pressure conditions becomes more attractive [21].

Due to the lack of specific functional groups in silica aerogels, the introduction of functional groups plays a crucial role in the adsorption of metal ions [22,23]. It has been widely reported that amine functionalized aerogel can be used as adsorbent to remove heavy metal ions from wastewaters [24]. Wang et al. [25] prepared pectin-based aerogels (PPEAs) by incorporating polyethylenimine (PEI) showing an excellent adsorption ability for lead-containing wastewater. Alyne et al. [26] reported that the lead removal efficiency of amine-functionalized silica aerogel was significantly improved after amine functionalization, and the removal efficiency was higher than 90%.

In view of the fact that traditional explanations of the adsorption mechanisms based on explicit correlation analysis, mainly through experimental tests, characterizations and classical models, are not comprehensive [27–30]. Meanwhile, the environmental impact of the aerogel preparation process has been much more rarely studied. In this work, Density Functional Theory (DFT) and Life Cycle Assessment (LCA) are therefore used to investigate the mechanisms of intermolecular interactions in the removal of pollutants by adsorbents and the environmental impact of adsorbents preparation, respectively. DFT is a molecular dynamics method that realistically reflects the thermodynamic properties of fluids in the pores of porous materials. It not only provides a microscopic model of adsorption, but also reflects the pore size distribution more accurately than conventional thermodynamic methods [31]. LCA is an environmentally and health-based method for quantifying emissions, resource consumption, and associated environmental and health impacts of products, services, and assets [32]. Previous applications include food production, electricity generation and dynamic life. Nevertheless, LCA started to be involved in the adsorbents sector in recent years, with a progress in a series of international standards development [33].

Based on the above considerations, mesoporous amino functionalized silica aerogels (MASA-X) with high adsorption capacity were firstly designed at ambient pressure conditions for the adsorption of Pb (II) from contaminated water. Then, the morphology, microstructure, specific surface area, and chemical binding states of MASA-X were investigated. The performance of MASA-X for Pb (II) adsorption were explored, including solution pH effects, adsorption kinetics, adsorption isotherm, adsorption thermodynamics and reusability. And the adsorption mechanism of Pb (II) was explained by a combination of FTIR, XPS and DFT calculation. Finally, the environmental impact of the MASA-2 preparation process was identified through LCA method. The innovative contribution of this study is the comprehensive investigation of the preparation, adsorption effect, mechanism and environmental impact of mesoporous amino functionalized silica aerogels, thus demonstrating that it has great potential application in heavy metal ions removing field.

2. Material and methodology

2.1. Materials

Tetraethoxysilane (TEOS), N, N-dimethylformamide (DMF), ammonia (NH_4OH), hydrochloric acid (HCl), ethanol (EtOH), lead chloride ($PbCl_2$), n-hexane were purchased from Xian Chemical Reagent Co. Ltd. 3-aminopropyl triethoxysilane (KH550) was supplied by Shanghai Aladdin Biochemical Technology Co. Ltd. The chemicals and reagents were analytical grade and were used without further purification.

2.2. Preparation of mesoporous amino functionalized silica aerogels (MASA-X)

The MASA-X samples were synthesized by a novel method eliminating the step of alkaline catalysis. Silica gel was prepared by sol-gel method, TEOS was used as precursor, HCl aqueous solution was used as catalyst, and ethanol was used as solvent. First, 10 mL TEOS was dissolved in ethanol with string. Then, 0.1 M HCl solution was added to adjust pH = 3 (all water was replaced by 0.1 M HCl solution), stirred and heated to 60 °C for reflux reaction for 2 h. After cooling to room temperature, 1.73 mL DMF was added and stirred for 15 min. And then KH550 was added into ethanol and stirred to obtain a uniform solution with a volumetric ratio of 1:10, the silica sol obtained above was added into the mixed solution with vigorous stirring for 30 s and transferred into a mold for gelation. The wet gels were obtained in 2 min. After the gel was formed, it was aged for 24 h with ethanol, then used ethanol to exchange 6 times within 48 h to remove redundant water and residual organic compounds, and then exchanged with n-hexane 4 times in 48 h in a water bath at 40 °C. Finally, the mesoporous amino silica aerogels (MASA-X) were obtained by drying the wet gel at 40 °C for 48 h under ambient pressure drying (APD). The molar ratios of n(TEOS): n(EtOH): n(H_2O): n(DMF) were 1 : 10: 16 : 0.5. According to the molar ratios of n(KH550): n(TEOS) ranging from 0.5, 1.0, 1.5 to 2.0, the synthesized samples were named as MASA-1, MASA-2, MASA-3 and MASA-4, respectively. MASA-2 is selected as a representative for subsequent DFT and LCA studies as it demonstrates optimal adsorption performance.

2.3. Characterizations

SEM morphology was observed on a scanning electron microscopy (Hitachi S-4800, Japan). Fourier transform infrared (FTIR) spectroscopy was provided by Nicolet 5700 spectrometer to analyze the functional groups on the surfaces of aerogels. X-Ray Diffraction (XRD) patterns of the samples were performed by using a D8 ADVANCE diffractometer. The specific surface area (S_{BET}) was measured by a NOVA 2200 analyzer using the Brunauer-Emmett-Teller method. The X-ray photoelectron spectroscopy analysis was obtained using an ESCALAB 250 (USA) instrument to analyze the chemical binding states of aerogels before and after adsorption. The Pb (II) concentrations were measured by atomic absorption spectrophotometry (AAS, WFX-120, Beijing Rayleigh Analytical Instrument Co., Ltd.).

2.4. Adsorption experiments

Adsorption experiments were carried out in the 50 mL centrifuge tube with 20 mL 50 mg/L Pb (II) solution using 0.5 g/L adsorbent. The effect of pH on Pb (II) adsorption was investigated by adjusting the initial pH from 1 to 6 using 0.1 M HCl and 0.1 M NaOH solutions. Adsorption kinetic experiments were investigated at different times from 10 min to 480 min, adsorption isotherm experiments were carried out in different initial concentration of Pb (II) with Pb (II) concentration varied from 10 mg/L to 1000 mg/L, and the adsorption thermodynamics of Pb (II) were also performed under different temperatures from 293 K to 313 K. The adsorption cycle experiment was carried out eight times. After each adsorption, the saturated adsorbents were added in 25 mL 0.1 M HCl solution with stirring for 180 min for desorption, and the next adsorption test was conducted. Each experiment was repeated three times and the average value was used in the results. The removal efficiency (%) and adsorption capacity (q, mg/g) of Pb (II) were calculated by the following Eqs. (1) and (2):

$$\varphi = \frac{c_0 - c}{c_0} \times 100\% \quad (1)$$

$$q = \frac{(c_0 - c) \times v}{w} \quad (2)$$

Where c_0 (mg/L) and c (mg/L) are the concentration of Pb (II) at initial and time t, respectively. v (L) is the volume of solution, w (g) is the dosage of adsorbent.

2.5. DFT calculation

The DFT calculations were conducted with Gauss 09 software [34]. The calculation was carried out using the B3LYP exchange-related hybrid functions in the ground state for the simulations [35]. Geometry optimization and frequency calculations were carried out using the LanL2DZ basis set for Pb atom and 6–31g(d) for the other atoms. And a larger basis set combination was used for the singlet point energy calculation, using the LanL2DZ basis set for Pb atom and 6–311 g(d, p) for the other atoms [36–38]. The adsorption energy (E_{ads}) can be calculated as given in Eq. (3) [39,40].

$$E_{ads} = E_{total} - (E_{adsorbent} + E_{metal}) \quad (3)$$

where E_{total} refers to the total energy associated with the adsorption of Pb (II) on MASA-2, $E_{adsorbent}$ implies the energy of MASA-2 and E_{metal} describes the energy of individual heavy metal Pb atom, respectively.

2.6. Life Cycle Assessment (LCA)

2.6.1. Goal and scope definition

Life Cycle Assessment (LCA) is a valuable tool for evaluating the environmental footprint of any product during its existence. This investigation used the LCA methodology to identify and characterize the environmental impacts associated with the production of 1 kg of mesoporous amino functionalized silica aerogels (MASA-2). The guidelines in the ISO 14044 standard [41] were used to calculate the impact on the environment. By analyzing the contribution of each material used in the production of MASA-2, environmental hotspots were identified and additional environmentally effective production strategies aimed at reducing the negative impact on sustainability are proposed. These insights may contribute to the popularity of MASA-2 in the absorbent market.

This work provided a cradle-to-grave LCA with system boundaries that included the production and transport of the raw materials that make up the MASA-2 and the preparation of the MASA-2, as shown in Fig. 1. The transport distance for raw materials was based on the average distance of 181 km for cargo transport in China. As there was no environmental impact during the use phase, no treatment was required during the end-of-life phase. This work did not consider the use and end-of-life phases.

2.6.2. Life cycle inventory analysis

Inventory analysis plays a key role in the whole assessment, revealing all the inputs and outputs of the entire synthesis process. Based on the boundary mentioned above, the inventory was collected and recorded from experiments conducted in our laboratory described in section 2.2. and previous literature. The calculations were conducted in eFootprint and the Ecoinvent database v.3.1 and CLCD were accessed for all data in the Life Cycle Inventory (LCI). This work presumed the use of a global average electricity mix as the electricity supply for production. The LCI for MASA-2 is shown in Table 1.

2.6.3. Life cycle impact assessment

According to Ferrão [42], the choice of evaluation method must be related to the choice of environmental impact category. In this work, the method used was based on intermediate indicators that focused on environmental loads and final consequences. The CML 2001method (developed in the Netherlands by the Institute of Environmental Sciences of the Leiden University) was used, with categories such as: Global Warming Potential (GWP); Acidification Potential (AP), Abiotic Depletion Potential (ADP), Eutrophication Potential (EP), Ozone Depletion Potential (ODP), and Photochemical Ozone Creation Potential (POFP). Meanwhile, a category for Primary Energy Demand (PED) has been added, based on the Cumulative Energy Demand (CED) approach.

3. Results and discussion

3.1. Characterization

Fig. 2 shows the SEM images of MASA-X samples synthesized with the different molar ratios (KH550/TEOS). All samples present the porous structure, which is derived from accumulation of nanoparticles and the growth of agglomerates is controlled by controlling the molar ratios of KH550/TEOS. At a molar ratio (KH550/TEOS) of 0.5, the skeleton structure of amino aerogel is composed of secondary particles with some clusters due to incomplete reaction, which contributed to the formation of the aerogel skeleton consisting of small silica agglomerates with dense porosity. As the molar ratio (KH550/TEOS) increase to 1.0, the surface of skeleton becomes rougher and forms a uniform porous morphology with more tightly connected secondary particles. Note that the secondary particle clusters become larger. With the molar ratio (KH550/TEOS) further increase, the size of pores which originated from accumulation of nanoparticles increase apparently, resulting in larger spherical agglomerates (Fig. 2c and **d**). The particle size of agglomerates derived from the polycondensation reactions between TEOS and KH550 increase with the KH550 ratio increasing, and the pores possess three-dimensional connection microstructure due to nanoparticles

Table 1
The LCI of 1 kg MASA-2.

	Mass	Unit
Raw material input		
TEOS	0.47	kg
Ethanol	20	kg
HCl	7.58	g
DMF	0.08	kg
KH550	0.49	kg
n-Hexane	13.86	kg
Water	0.64	kg
Energy input		
Electricity	2	kWh
Transportation	181	km
Output		
MASA-2	1	kg

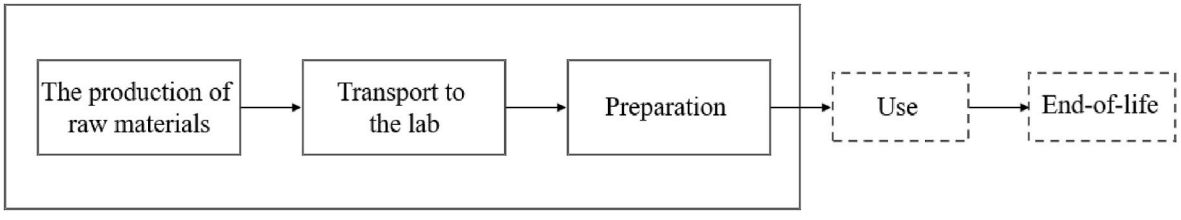

Fig. 1. Stages of MASA-2 considered in this study.

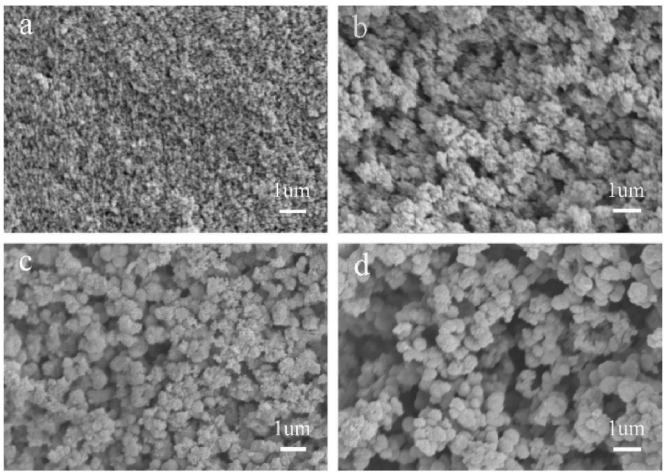

Fig. 2. SEM images of MASA-X synthesized at different KH550/TEOS molar ratios. (a) 0.5; (b) 1.0; (c) 1.5; (d) 2.0.

accumulation effect.

The small angle XRD patterns (Fig. 3a) can be used to characterize the structure of the MASA-X samples. All amino-functionalized silica aerogels with different amino group loadings exhibited two diffraction peaks that can be indexed to (100) and (200) reflections associated with two-dimensional hexagonal mesostructure, which is consistent with the results reported in the literature [43,44]. However, there was a gradual reduction in the intensity of the (100) diffraction peak and a gradual disappearance of the (200) diffraction peak as the increase amount of KH550, suggesting that the use of the organosilicon source had influenced the formation of the mesoporous structure and had resulted in a gradual decrease in the ordered of the mesostructured [45]. The wide angle XRD patterns are shown in Fig. 3b. The XRD peaks of samples present similar broadened diffraction peak at about 22°, corresponding to the typical amorphous silica structure [46]. With the increasing of the KH550/TEOS molar ratio, the diffraction intensity of amorphous silica gradually weakened, indicating that hydrolysis reaction and condensation reaction of TEOS are preferred to form amorphous structure.

FTIR spectra for MASA-X with different KH550/TEOS molar ratios are displayed in Fig. 4. The peaks at 460 cm^{-1}, 781 cm^{-1} and 1054 cm^{-1} are ascribed to the Si–O–Si bending vibration peak, symmetric vibration peak and asymmetric vibration peak, respectively. The peak at 2929 cm^{-1} is designated as the vibration of C–H [47], and the band at 1649 cm^{-1} is attributed to the O–H of adsorbed water. The peak at 1564 cm^{-1} is associated with N–H bending vibration peak. The peak at 3431 cm^{-1} is ascribed to the O–H band and N–H bond. Obviously, the adsorption intensity of N–H, C–H and Si–O–Si increase with the molar ratio (KH550/TEOS) increasing, indicating that silane coupling reagents

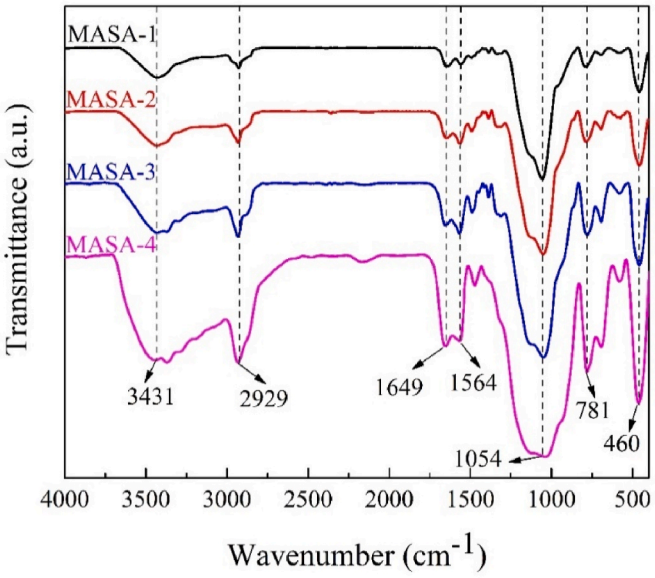

Fig. 4. FTIR spectra of MASA-X.

KH550 and TEOS have good compatibility.

Fig. 5 presents the N_2 adsorption-desorption isotherms of MASA-X. All samples possess type IV curves feature, and the hysteresis loops appears at relative pressures between 0.70 and 0.95, which indicating that mesoporous and macroporous structures are formed in the sample [48]. The corresponding pore size distribution can be seen in the inset in Fig. 5. As shown, the specific surface areas of MASA-1, MASA-2, MASA-3 and MASA-4 are calculated to be 169.74 m^2/g, 118.42 m^2/g, 82.44 m^2/g and 53.66 m^2/g, respectively. And the pore sizes of MASA-1, MASA-2, MASA-3 and MASA-4 were 17.96 nm, 18.79 nm, 26.55 nm and 58.17 nm, respectively. The pore sizes of MASA-1, MASA-2, MASA-3 and MASA-4 can be observed to be getting progressively larger. It can be concluded that the amino silane coupling agent react with the incomplete ethyl orthosilicate to form larger particles, and average diameter of pores increases rapidly in this process due to the pores plugging [49,50]. These results confirmed that excessive amino silane coupling agent had been successfully grafted onto the skeleton of aerogels.

The elemental analysis data of MASA-1, MASA-2, MASA-3 and MASA-4 are summarized in Table S1. It is clear that the nitrogen content of MASA-1, MASA-2, MASA-3 and MASA-4 samples gradually increase with the increase of the mole ratio of amino silane coupling agent. This suggests that the mole ratio of amino silane coupling agent added directly determines the loading amount of KH550 in the MASA-X samples, and further confirms the successful preparation of amino functionalized silica aerogels.

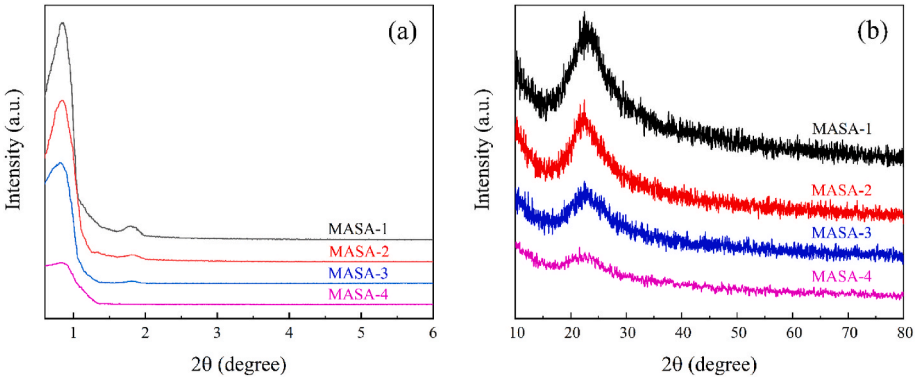

Fig. 3. XRD patterns of MASA-X. (a) small-angle; (b) wide-angle.

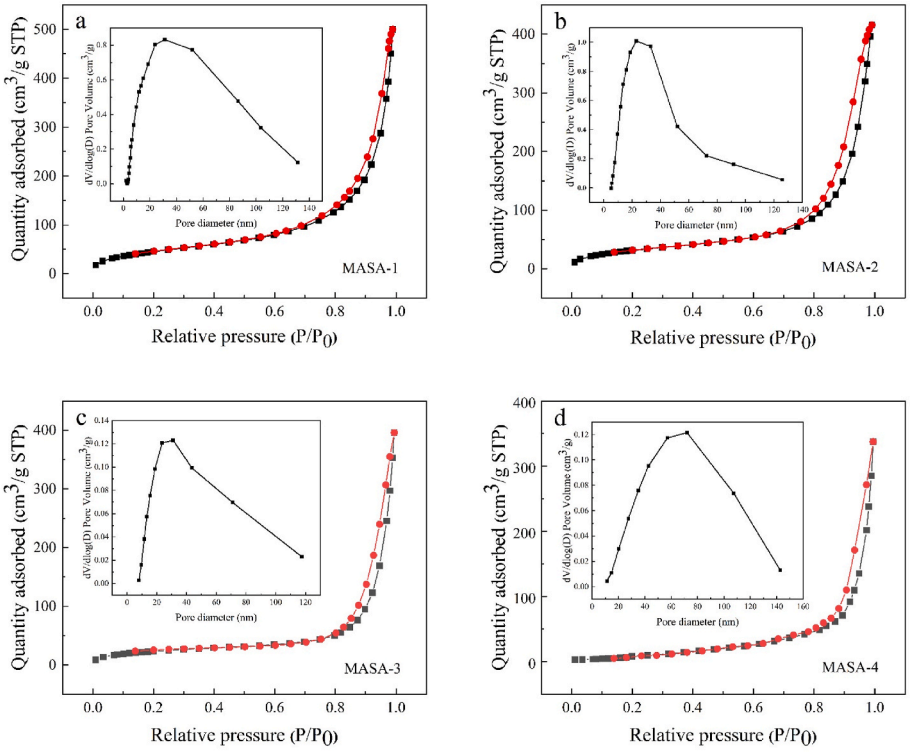

Fig. 5. N_2 adsorption-desorption isotherms of MASA-X.

3.2. Adsorption properties

3.2.1. Effect of pH

The pH of the solution has a significant effect on the adsorption of Pb (II) by changing the charge on the surface of the adsorbent [51]. The effects of pH (1–6) on the removal efficiency of Pb (II) is shown in Fig. 6. At low pH, the surface of the amino adsorbent is protonated and there is electrostatic repulsion between the adsorbent and Pb (II), resulting in a low removal efficiency of Pb (II). When the pH value increase from 1 to 6, the removal efficiency of Pb (II) gradually increase because the protonated amino groups gradually deprotonated and reached a maximum at pH 5. The removal efficiency of Pb (II) increase slightly when the pH is exceeded 5, and the Pb (II) ions in solution will be precipitated as Pb $(OH)_2$ state while the pH is above 6. Therefore, it is concluded that the adsorption process is pH–dependent.

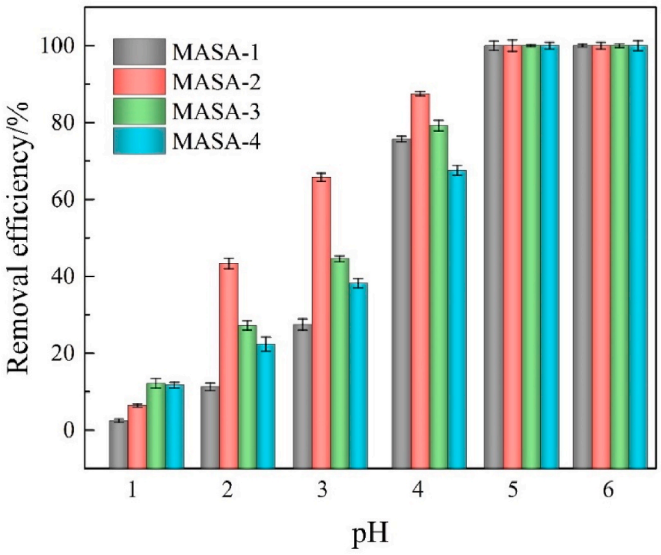

Fig. 6. The effect of pH on the removal efficiency of Pb (II).

The pH of point of zero charge (pH_{pzc}) is performed by the ΔpH method [52,53]. Fig. S1 shows the point of zero charge (pzc) of MASA-X at different pH. The pH_{pzc} of the four aerogels are in the ranged of 5.6–6.0. When the pH value is lower than the pH_{pzc}, the surface of aerogels present positive charged, indicating the existence of protonated binding sites on the aerogels surface, which hinders the adsorption of heavy metals. However, while the pH value is higher than pH_{pzc}, the surface of the aerogel is negative charged, indicating that in the deprotonation of the amino group, which is favorable for the adsorption of metal ions from solution.

3.2.2. Adsorption kinetics

The adsorption capacity of four adsorbents are plotted against adsorption time in Fig. S2. A rapid adsorption is observed in the initial stage, then followed by a level-off to reach equilibrium adsorption. The equilibrium adsorption times of MASA-1, MASA-2, MASA-3 and MASA-4 were 120 min, 60 min, 20 min and 20 min, respectively. It can be seen that the diffusion of Pb (II) into the pores of aerogel is slower than the interactions between Pb (II) and adsorbents.

In order to explore the adsorption process and possible adsorption mechanisms, a series of kinetic studies were performed. The results are presented in Fig. 7 and the corresponding parameters are summarized in Table 2. Furthermore, the experimental data are fitted using four kinetic models: Pseudo-first-order kinetic model, Pseudo-second-order kinetic model, Elovich kinetic model and Intraparticle diffusion model. The linear form of the four models is represented by the following equation [54,55]:

$$\ln(q_e - q_t) = -k_1 t + \ln q_e \quad (4)$$

$$\frac{t}{q_t} = \frac{t}{q_e} + \frac{1}{k_2 q_e^2} \quad (5)$$

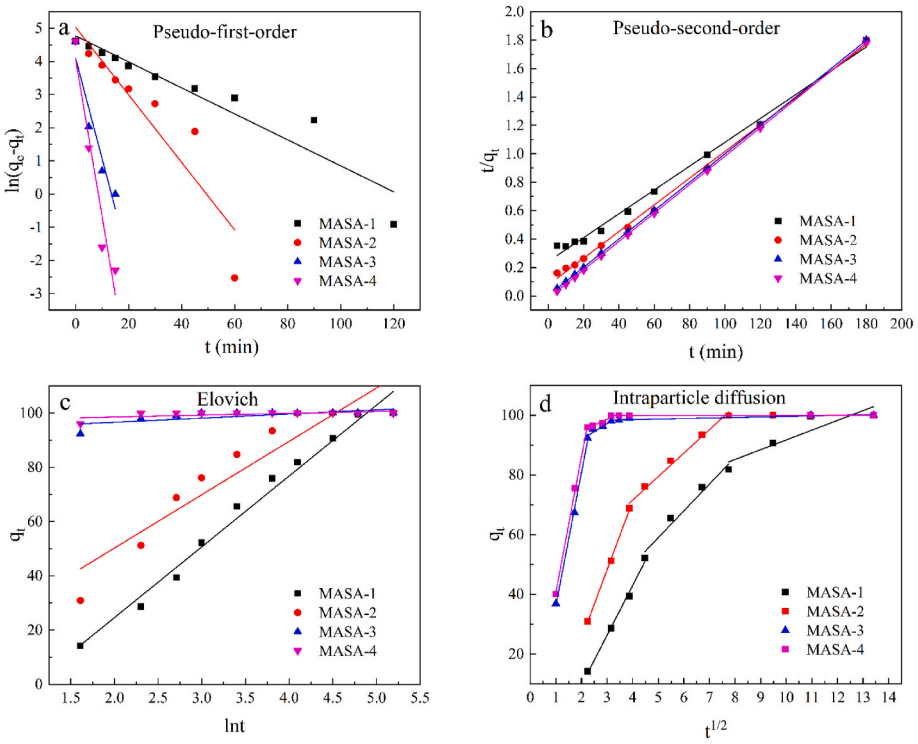

Fig. 7. Adsorption kinetics modelling of Pb (II) adsorption on MASA-X.

Table 2
Adsorption kinetic parameters of Pb (II) adsorption on MASA-X.

Kinetic models	Parameters	MASA-1	MASA-2	MASA-3	MASA-4
Pseudo-first-order	k_1 (min^{-1})	0.03918	0.1019	0.3030	0.4746
	q_e (mg/g)	118.04	153.59	60.75	59.25
	R^2	0.8932	0.8373	0.8914	0.9096
Pseudo-second-order	k_2 (g/(mg·min)	0.0002909	0.001147	0.0656	0.2019
	q_e (mg/g)	119.05	105.26	100.10	100
	R^2	0.9969	0.9989	1	1
Elovich	α (mg/(mg·min)	9.0654	34.2703	6.8761 $\times 10^{26}$	2.2470 $\times 10^{61}$
	β (mg/g)	0.03832	0.05087	0.6561	1.4582
	R^2	0.9804	0.8705	0.4699	0.3079
Intraparticle diffusion	k_{p1} (mg/(g·$min^{1/2}$)	16.7031	23.0817	44.6484	45.4086
	R^2	0.9943	0.9988	0.9976	0.9977
	k_{p2} (mg/(g·$min^{1/2}$)	8.9733	7.8799	5.4833	3.9656
	R^2	0.9698	0.9877	0.9102	0.9006
	k_{p3} (mg/(g·$min^{1/2}$)	3.2716	0.0123	0.1772	0.0155
	R^2	0.8302	0.5437	0.8543	0.7962

$$q_t = \frac{1}{\beta}\ln t + \frac{1}{\beta}\ln(\alpha\beta) \tag{6}$$

$$q_t = k_p\sqrt{t} + C \tag{7}$$

Where q_t (mg/g) and q_e (mg/g) are the adsorption capacity of Pb (II) at time t (min) and at equilibrium, respectively, and k_1 (min^{-1}), k_2 (g/(mg·min) and k_p (mg/(g·$min^{1/2}$) are the rate constant of the pseudo-first-order model, pseudo-second-order model and intra-particle diffusion model, respectively. C is constant. α (mg/(mg·min) and β (mg/g) are the initial elovich rate constant and desorption elovich rate constant, respectively.

By comparing and analyzing the data in Table 2, it can be concluded that the adsorption kinetics were better described with the pseudo-second-order kinetic model than other three kinetic models, with higher fitting correlation coefficients (R^2), and the fitting correlation coefficients (R^2) of pseudo-second-order models are all greater than 0.996, and the equilibrium adsorption capacities of the four samples calculated by pseudo-second-order model were 119.05 mg/g, 105.26 mg/g, 100.10 mg/g and 100.00 mg/g for MASA-1, MASA-2, MASA-3 and MASA-4 respectively, which were very close to the results of the adsorption experiments (all MASA-X samples had a saturation adsorption capacity of 100.00 mg/g). Furthermore, the intraparticle diffusion model also demonstrated a good fitting to the experimental data, and the order of adsorption rates for all samples of MASA-X was $k_{p1} > k_{p2} > k_{p3}$. The first rapid adsorption was ascribed to the diffusion of Pb (II) ions from the liquid phase to the exterior surface of the solid adsorbent, during this period, Pb (II) was readily adsorbed to the exterior surface of the adsorbent due to membrane diffusion. In the second stage, there was a drop in the adsorption rate due to the gradual diffusion of Pb (II) ions into the internal pores of the adsorbent. Finally, the intraparticle diffusion rate exhibited a very low rate as the adsorption sites reached saturation. The intraparticle diffusion model revealed that multiple processes were engaged in the adsorption, which was consistent with previous literature [50]. In summary, it can be interpreted that the adsorption behavior of Pb (II) on MASA-X is mainly controlled by chemisorption [56,57].

3.2.3. Adsorption isotherm

The adsorption properties of MASA-X are evaluated by testing the adsorption capacity of MASA-X at different initial concentrations of Pb (II) at room temperature. As can be observed from Fig. S3, the adsorption capacity gradually increases with the increasing of initial concentration of Pb (II), and eventually reaching equilibrium. Adsorption isotherms play a very important role in optimizing experimental design and illustrating the interrelationships between adsorbates and adsorbents. Langmuir, Freundlich, Temkin, and Dubinin-Radushkevich (D-R) isotherm models are used to describe the adsorption of Pb (II) onto amino aerogel. These corresponding models are expressed as follows

[58,59].

Langmuir isotherm model:

$$\frac{c_e}{q_e}=\frac{c_e}{q_m}+\frac{1}{q_m K_L} \tag{8}$$

Freundlich isotherm model:

$$\log q_e = n \log c_e + \log K_F \tag{9}$$

Temkin isotherm model:

$$q_e = B_T \ln K_T + B_T \ln c_e \tag{10}$$

Dubinin-Radushkevich isotherm model:

$$\ln q_e = -K_{DR}\varepsilon^2 + \ln q_{DR} \tag{11}$$

$$\varepsilon = RT \ln\left(1+\frac{1}{c_e}\right) \tag{12}$$

$$E=\frac{1}{\sqrt{2K_{DR}}} \tag{13}$$

where q_m (mg/g) is the maximum adsorption capacity of the adsorbent, K_L (L/mg), K_F ((mg/g)/(mg/L)^n), K_T (L/g) and K_{DR} (mol^2/kJ^2) are the equilibrium constant of Langmuir isotherm model, Freundlich isotherm model, Temkin isotherm model and Dubinin-Radushkevich (D-R) isotherm model, respectively. n is the Freundlich intensity parameter. B_T is the Temkin constant. ε is the Polanyi potential, E (kJ/mol) is the mean adsorption energy, R (8.314 J/(mol·K)) is the gas constant, T (K) is the Kelvin temperature.

The linear fitting results were shown in Fig. 8 and Table 3. Compared with the other models, the Langmuir model has a higher correlation coefficient, and its calculated theoretical maximum adsorption amounts for MASA-1, MASA-2, MASA-3 and MASA-4 were 444.4 mg/g, 628.93 mg/g, 549.45 mg/g and 286.53 mg/g, respectively, which was much closer to the experimental obtained maximum adsorption amounts of 442.35 mg/g, 624.28 mg/g, 540.62 mg/g and 288.16 mg/g for MASA-1, MASA-2, MASA -3 and MASA-4, respectively, indicating that the Langmuir model was more suitable to describe the adsorption of Pb (II) and the adsorption process belongs to monolayer adsorption. In addition, a comparison of the MASA-X adsorbents with other adsorbents reported in recent years was presented in Table 4. Obviously, MASA-2 displayed excellent adsorption performance with a greater adsorption capacity and considerably faster adsorption equilibration times. Furthermore, the n values calculated form the Freundlich equation are in the range of $0 < n < 1$, suggesting that the adsorption of Pb (II) is favorable. In addition, the Temkin isotherms was also in good agreement with the adsorption experimental data, indicating that the electrostatic interactions may affect the adsorption of heavy metal ions [58,60]. The E values calculated from the Dubinin-Radushkevich equation are 37.3096 kJ/mol, 62.4688 kJ/mol, 43.4697 kJ/mol and 44.7814 kJ/mol, respectively. According to relevant literatures [61,62], if the E value is lower than 8 kJ/mol, it belongs to physical adsorption, if the E value is between 8 kJ/mol and 16 kJ/mol, then the adsorption process is caused by the ion exchange, and if the E value is higher than 16 kJ/mol, it belongs to chemisorption. Therefore, the adsorption of Pb (II) by MASA-X belongs to chemical adsorption.

3.2.4. Adsorption thermodynamics

The effect of temperature on the adsorption of Pb (II) is also carried out in the range of 293–313 K (Fig. S4). Obviously, the adsorption capacity of Pb (II) on MASA-X gradually increases with the increase of temperature. Thermodynamic analysis can describe whether the adsorption process is spontaneous and the stability of the adsorbed phase. The thermodynamic parameters such as enthalpy change(ΔH^0), entropy change(ΔS^0) and Gibbs free energy change(ΔG^0) in the adsorption process can be obtained from the following equations [69,70].

$$\Delta G^0 = -RT \ln k_c \tag{14}$$

$$k_c = \frac{c_\partial}{c_e} \tag{15}$$

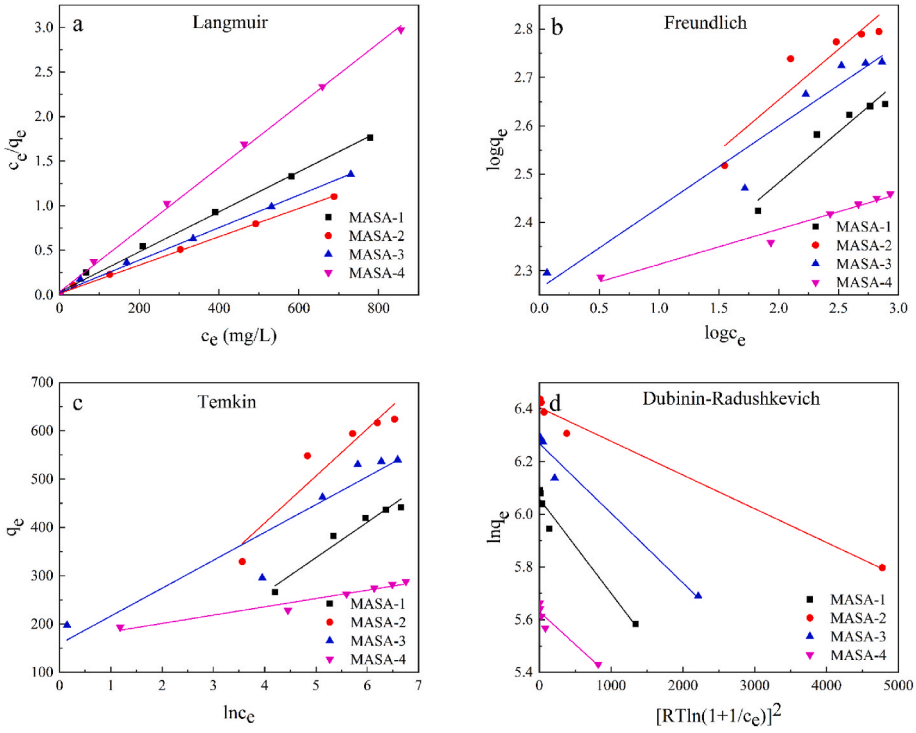

Fig. 8. Adsorption isotherms models for Pb (II) adsorption on MASA-X.

Table 3
Adsorption isotherms fitting parameters for Pb (II) adsorption on MASA-X.

Isotherms models	Parameters	MASA-1	MASA-2	MASA-3	MASA-4
Langmuir	k_L (L/mg)	0.06637	0.09642	0.07197	0.1026
	q_m (mg/g)	444.44	628.93	549.45	286.53
	R^2	0.9960	0.9978	0.9962	0.9985
Freundlich	k_F ((mg/g)/(mg/L)^n)	115.5447	171.4905	183.1724	174.0003
	n	0.2099	0.2097	0.1684	0.07273
	R^2	0.9067	0.8182	0.92792	0.9626
Temkin	k_T (L/g)	0.6798	1.2178	15.6520	16725.6709
	B_T	73.1395	97.4467	57.7116	17.1701
	R^2	0.9387	0.8644	0.8725	0.9415
Dubinin-Radushkevich	k_{DR} (mol^2/kJ^2)	3.5919×10^{-4}	1.2813×10^{-4}	2.6460×10^{-4}	2.4933×10^{-4}
	q_{DR} (mg/g)	427.99	604.93	527.76	278.90
	E (kJ/mol)	37.3096	62.4688	43.4697	44.7814
	R^2	0.9547	0.9812	0.9639	0.8724

Table 4
Comparison of the maximum adsorption capacities (q_m) of MASA-X adsorbents with other adsorbents.

Adsorbents	conditions	q_m (mg/g)	Reference
A-GO	c_0- 25–250 mg/L; pH-6.5; T-313 K; dose- 10 mg; time- 120 min	408	[63]
Fe_3O_4@BC/APTES	c_0- 10–100 mg/L; pH-6.8; T-323 K; dose- 10 mg; time- 60 min	64.92	[64]
DAS2-AT	c_0- 50–300 mg/L; pH-6; T-323 K; dose- 50 mg; time- 360 min	203.2	[65]
PAMAM@UiO-66-NH_2	c_0- 100–1000 mg/L; pH-4; T-298 K; dose- 10 mg; time- 50 min	334.32	[66]
HTMT	c_0- 100–600 mg/L; pH-5; T-298 K; dose- 10 mg; time- 60 min	540.5	[67]
ACEA-14	c_0- 10–120 mg/L; pH-6; T-298 K; dose- 0.4 g/L; time- 480 min	122.7	[68]
Fe_3O_4@TATS@ATA	c_0- 25–400 mg/L; pH-5.7; T- 298 K; dose- 20 mg; time- 150 min	205.2	[61]
MASA-1	c_0- 10–1000 mg/L; pH-5; T- 298 K; dose- 0.5 g/L; time- 120 min	444.4	This work
MASA-2	c_0- 10–1000 mg/L; pH-5; T- 298 K; dose- 0.5 g/L; time- 60 min	628.93	This work
MASA-3	c_0- 10–1000 mg/L; pH-5; T- 298 K; dose- 0.5 g/L; time- 20 min	549.45	This work
MASA-4	c_0- 10–1000 mg/L; pH-5; T- 298 K; dose- 0.5 g/L; time- 20 min	286.53	This work

$$\ln k_c = -\frac{\Delta H^0}{RT} + \frac{\Delta S^0}{R} \tag{16}$$

Where k_c is the distribution coefficient, c_∂ (mg/L) is the concentration of heavy metal ions on the adsorbent surface. The ΔS^0 and ΔH^0 can be obtained from the intercept and slope by plotting lnk_c versus $1/T$ (Fig. 9). And the calculation results are listed in Table 5.

The negative values of ΔG^0 reveal that the adsorption of Pb (II) was a spontaneous process. And the absolute values of ΔG^0 increase with the increasing of temperature, indicating that Pb (II) adsorption was favorable at higher temperature. In addition, the positive values of ΔH^0 suggest an endothermic nature and the positive ΔS^0 values indicating that the randomness increasing at solid-liquid interface [71]. Meanwhile, the $T\Delta S^0$ values were always greater than ΔH^0, which indicates that the adsorption of Pb (II) on the adsorbents surface was the entropy-controlled process [72].

3.2.5. Reusability property

The reuse of adsorbents is a key issue for economics and environmental protection. After adsorption of Pb (II), the exhausted adsorbent was regenerated by HCl solution (0.1 mol/L), and the reusability of MASA-2 was evaluated in Fig. 10. After 8 consecutive adsorption-desorption cycles experiments, the Pb (II) removal efficiency of MASA-2 still remain 95.82%, indicating that MASA-2 has excellent cycling stability.

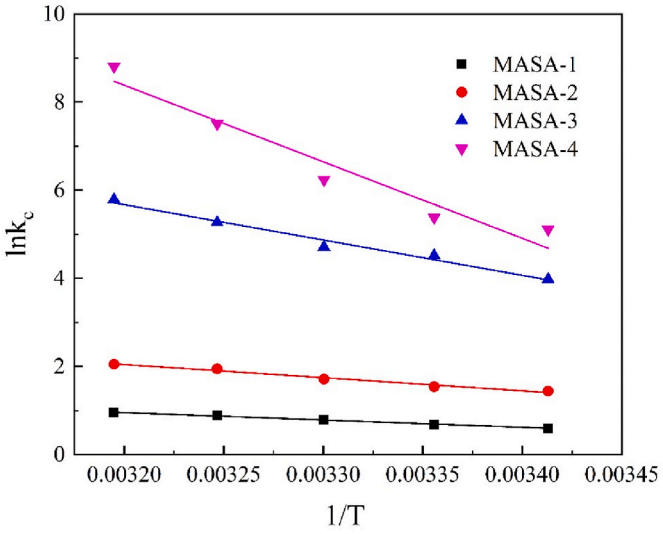

Fig. 9. The plots of lnk_c vs $1/T$ for Pb (II) adsorption onto MASA-X.

Table 5
Thermodynamic parameters for Pb (II) adsorption onto MASA-X.

Samples	T/K	$\triangle G^0$/(kJ/mol)	$\triangle H^0$/(kJ/mol)	$\triangle S^0$/(J/(mol·K)
MASA-1	293	−1.4490		
	298	−1.6930		
	303	−1.9980	13.8353	52.1815
	308	−2.2800		
	313	−2.458		
MASA-2	293	−3.5086		
	298	−3.8118		
	303	−4.3089	24.7767	96.2562
	308	−4.9794		
	313	−5.3360		
MASA-3	293	−9.6876		
	298	−11.1921		
	303	−11.8579	66.5678	260.1456
	308	−13.4786		
	313	−15.0661		
MASA-4	293	−12.4479		
	298	−13.3221	144.4788	532.0178
	303	−15.7143		
	308	−19.2183		
	313	−22.9124		

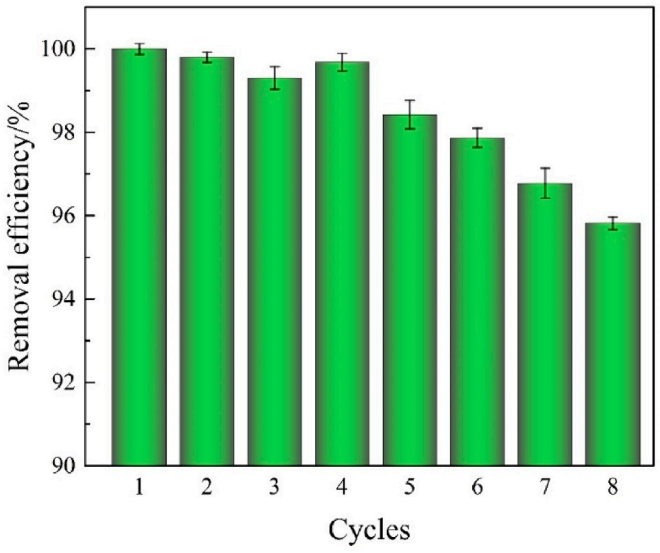

Fig. 10. The reusability study of MASA-2.

3.3. Adsorption mechanism

For comprehensive investigation the adsorption mechanism of Pb (II) onto MASA-2, FTIR technique is used to analyze MASA-2 before and after Pb (II) adsorption (Fig. S5). The characteristic adsorption peaks at 1564 cm^{-1} and 3431 cm^{-1} which are ascribed to the bending vibration and the stretching vibration of N–H bond in the sample MASA-2, respectively. After adsorption of Pb (II) by MASA-2, the characteristic peaks of N–H bond are shifted to 1569 cm^{-1} and 3436 cm^{-1}, respectively, because coordination adsorption of metal ions leads to the chemical environment changing. It can be inferred that the $–NH_2$ group is involved in this adsorption process due to the coordination bond formation between Pb (II) ions and NH_2 groups.

The XPS spectra of MASA-2 before and after Pb (II) adsorption were shown in Fig. 11. In the overall spectrum of MASA-2, there are five peaks at 285 eV, 149 eV, 102 eV, 399 eV, 532 eV corresponding to C 1s, Si 2s, Si 2p, N 1s and O 1s, respectively (Fig. 11a). After adsorption of Pb (II), a new peak of Pb 4f in the binding energy at 138 eV is observed in the sample, which confirms that Pb (II) is adsorbed onto MASA-2. The high resolution of Pb (II) binding energies at 142.8 and 137.9 eV can be assigned to Pb 4f5/2 and Pb 4f7/2, respectively [73], as shown in Fig. 11b. This suggests that Pb (II) is effectively existed on the surface of MASA-2. Fig. 11c exhibits the high-resolution C 1s spectra of MASA-2, three peaks at binding energy of 283.9 eV, 284.8 eV and 285.8 eV are ascribed to C–Si, C–C and C–N, respectively. After adsorption of Pb (II), the binding energy of C–Si (283.9 eV), C–C (284.8 eV) did not change, while the binding energy of C–N (285.3 eV) is remarkably decreased after binding to Pb (II) (Fig. 11e). When adsorption of Pb (II) ions occurs on the surface of MASA-2, the lone pair electron of N atom is combined with the empty orbit of Pb (II) ions to form a new chemical coordination bond, and the bond energy of C–N decrease simultaneously. The binding energy of N 1s are observed at 399.1 eV and 401.1 eV, which are attributed to $–NH_2$ and $–NH_3^+$, respectively (Fig. 11d). After adsorption of Pb (II), the binding energy of $–NH_2$ and $–NH_3^+$ are remarkably shifted to 400.1 eV and 402.2 eV, respectively (Fig. 11f), which is due to the lone pairs of N coordinate with Pb (II) ions lead to the surrounding electron cloud density decreased and the binding energy increased [74]. The XPS results and the FTIR spectra are confirmed that N atom participated in coordination with Pb (II).

The optimized molecular model of MASA-2 for the binding of Pb (II) was depicted in Fig. 12. The DFT results demonstrated that the adsorption binding energy corresponding to the adsorption configuration was −6.32 kcal/mol. Notably, there is a tendency for the molecule to interact with Pb (II) by chelation of a monodentate nitrogen atom ligand with Pb (II) at a Pb–N bond distance of 2.498 Å, which is similar to the findings of Zhao et al. [75]. This demonstrated that the Pb (II)–N interaction facilitated the uptake of Pb (II) on MASA-2, which is consistent with the XPS results. HOMO and LUMO depict the donating and acquiring electrons ability respectively. The size of $E_{gap} = E_{LUMO} - E_{HOMO}$ reflects the ability of electrons to make the jump from occupied orbitals to empty orbitals, and to some extent represents the ability of the molecule to participate in chemical reactions. If E_{gap} is larger, indicating that the molecule is more stable due to the fact that it is less readily to be excited [76]. The changes of HOMO and LOMO before and after the adsorption of Pb (II) on MASA-2 and its gap energy (E_{gap}) are presented in Fig. 13. A clear view can be found that the LUMO of MASA-2 is mainly distributed on the Si–O–Si backbone, while the HOMO is partially located on the -NH2 group. However, it is noteworthy that both LUMO and HOMO were significantly altered after Pb (II) adsorption, demonstrating that Pb (II) was successfully bound on MASA-2. In addition, the E_{gap} of MASA-2 was found to decrease when Pb (II) was adsorbed, which suggested that the previous steady structure was disrupted by the adhering Pb (II) [77]. XPS analysis and DFT calculation results point to a significant role of Pb (II)–N interactions in the adsorption behavior of Pb (II) on MASA-2.

3.4. Environmental impacts of MASA-2

As the results in section 3.2. show that MASA-2 exhibits better properties compared to other samples after adsorption and adsorption-desorption cycles, the LCA method is applied in this section to assess the environmental impact of producing 1 kg of MASA-2 adsorbent (Table 6). It can be seen that the highest impact value is achieved in the PED, i.e. 2385.4 MJ. Also, there is a higher production of greenhouse gases during the production process, which can lead to an increase in the global greenhouse effect. In addition to the two points mentioned above, the maximum value produced during the production of MASA-2 is only 0.19 in terms of AP, so the MASA-2 production process mainly affects GWP and PED.

In order to find a method that would enable further evaluation of the environmental impact of MASA-2 in production, all eight environmental impact indicators were normalized so that all factors for each impact profile were 100%. The results are shown in Fig. 14. It can be seen that all the materials required for production, ethanol and n-hexane are the most influential components. The contributions of ethanol to GWP, AP, ADP, EP, ODP, FOFP and PED are 72.23%, 63.49%, 46.67%, 29.36%, 45.42%, 53.83%, and 27.65% respectively; while the contributions of n-hexane are 9.11%, 19.13%, 32.62%, 22.77%, 46.58%, 38.69%, and 11.52%. In addition, Table 1 shows that the amounts of TEOS and KH550 are 0.47 kg and 0.49 kg, respectively, which are approximately 3.38% and 3.53% of the amount of n-hexane used, but contributed 4.98% and 8.35% to the GWP of the MASA-2 synthesizing phase. KH550 also exhibits a huge influence in terms of PED, accounting for 46.58% of the influence of all constituent materials.

In order to discover a way to synthesize MASA-2 with less environmental impact, the four raw materials mentioned above must be replaced or recycled. Ethanol and n-hexane are volatile and are heated during the production of MASA-2 thus evaporating the ethanol and n-hexane, techniques can be adopted to collect the evaporated ethanol and n-hexane. The recovery of ethanol and n-hexane will significantly change the environmental impact of MASA-2. The use of other silica sources such as sodium silicate (i.e., water glass) with less environmental impact than that of TEOS is worth pursuing [78]. To analyze the environmental impact of KH550, it can be explored in terms of its synthesis process, the reaction equation of which is shown below.

$$Si + CH_3CH_2OH \xrightarrow{cat.} HSi(OCH_2CH_3)_3 + H_2 \quad (17)$$

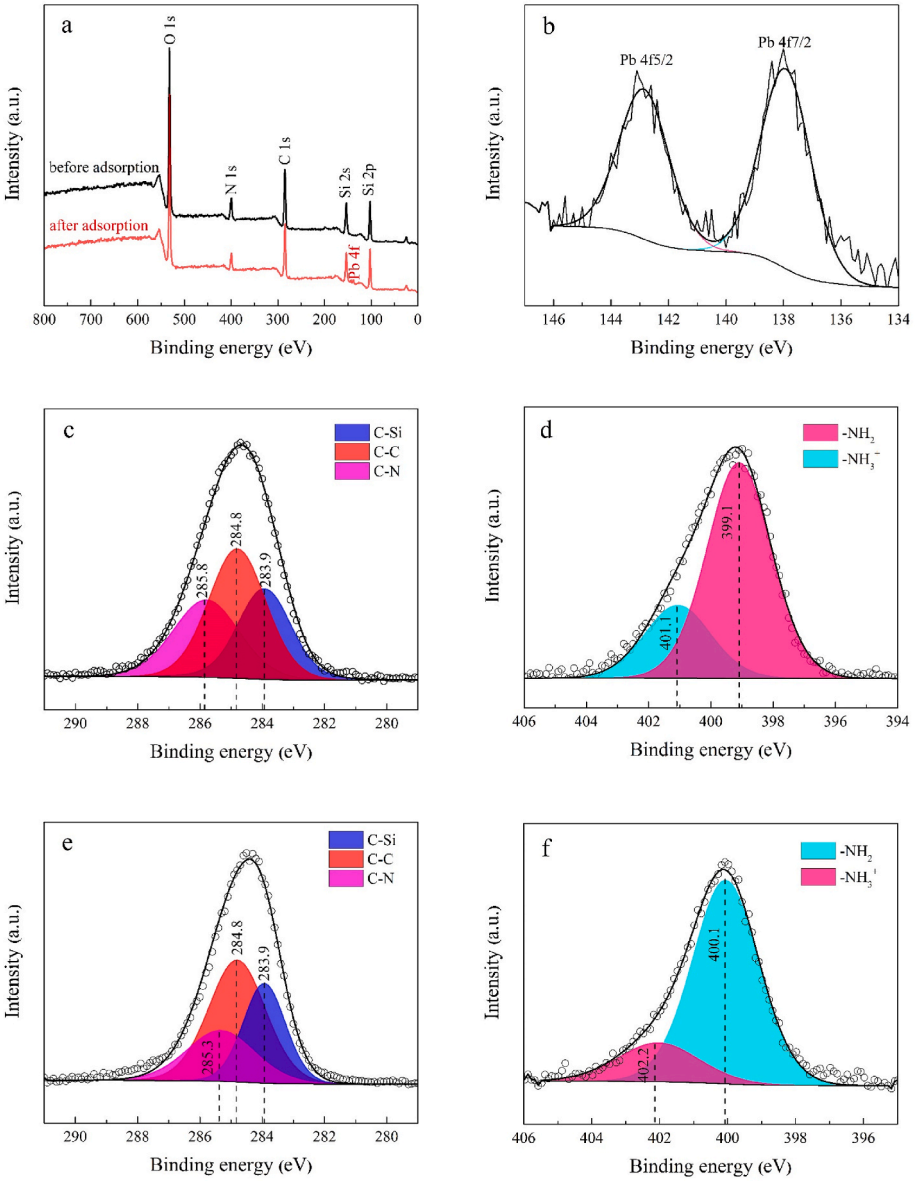

Fig. 11. XPS spectra of MASA-2: (a) overall spectrum before and after Pb (II) adsorption; (b) high resolution of Pb 4f; C1spectra before Pb (II) adsorption (c) and after Pb (II) adsorption (e); N 1s spectra before Pb (II) adsorption (d) and after Pb (II) adsorption (f).

$$ClCH_2CH=CH_2+HSi(OCH_2CH_3)_3\xrightarrow{cat.}ClCH_2CH_2CH_2Si(OCH_2CH_3)_3 \quad (18)$$

$$ClCH_2CH_2CH_2Si(OCH_2CH_3)_3+NH_3\xrightarrow{cat.}NH_2CH_2CH_2CH_2Si(OCH_2CH_3)_3+HCl \quad (19)$$

KH550 was obtained from allyl chloride, silicon, methanol, and ammonia over a catalyst. The impact of the catalyst on environmental factors was not considered during the synthesis as the catalyst was not involved in the reaction and could be recycled after the completion of the test. In order to understand the contribution of each component, the above indicators are normalized making all factors of each impact profile is 100% and the results are shown in Fig. 15. All the materials required for synthesis, ammonia is the most influential components. The contributions of ammonia to GWP, AP, ADP, EP, ODP, FOFP and PED are 89.82%, 60.20%, 96.47%, 95.12%, 12.68%, 34.85% and 98.86%, respectively. The search for an environmentally friendly material to replace the role played by ammonia in the synthesis of KH550 or a new synthesis method for KH550 that avoids the use of ammonia could therefore have a positive impact on the environment.

4. Conclusions

The mesoporous amino functionalized silica aerogels (MASA-X) with high adsorption capacity are prepared for the removal of Pb (II) ions from solution. Microstructure characterization and surface chemical composition analysis reveal a great deal of $–NH_2$ groups and porous structure existed in MASA-X. Based on previous reports [1,25,79–81], the present study demonstrates that the extensive presence of amino functional groups on the surface of the adsorbent plays a critical role in promoting the adsorption process. The adsorption kinetics and isotherms data are well fitted with the pseudo-second-order model and Langmuir model, both results prove that the adsorption process for Pb (II) onto MASA-X is mainly controlled by chemisorption reactions. The adsorption equilibrium of MASA-1, MASA-2, MASA-3 and MASA-4 are reached in 120 min, 60 min, 20 min and 20 min, respectively. And the maximum adsorption capacity of MASA-1, MASA-2, MASA-3 and

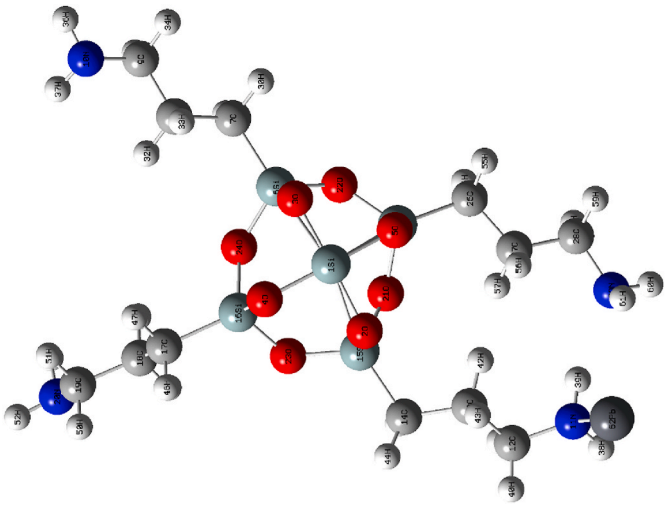

Fig. 12. The optimized geometric model of MASA-2 bonding to Pb (II).

MASA-4 are 444.4 mg/g, 628.93 mg/g, 549.45 mg/g and 286.53 mg/g, respectively. Thermodynamic studies show that the Pb (II) ions adsorption onto MASA-X are endothermic and spontaneous process. The adsorption efficiency of MASA-2 is remained 95.8% after eight adsorption-desorption cycles, indicating that it has excellent cycling stability. Combining FTIR, XPS and DFT computation, the N atom of $-NH_2$ in MASA-2 played a dominant role in providing the lone pair of electrons combined with Pb (II) to form the monodentate complex. At the end of this study the environmental impact of producing 1 kg of MASA-2 was investigated. By analyzing the contribution of various materials in the production of MASA-2, environmental hotspots are identified and proposed solutions, which are of great importance for the sustainability of MASA-2 production and the protection of the environment.

Table 6
The environmental impact of the production of 1 kg of MASA-2.

Category	Unit	Result
GWP	kg CO_2 eq	51.05
AP	kg SO_2 eq	0.19
ADP	kg antimony eq.	0.008
EP	kg PO_4^{3-}eq	0.03
ODP	kg CFC^{-11} eq	7.27E-06
POFP	kg NMVOC eq	0.16
PED	MJ	2385.4

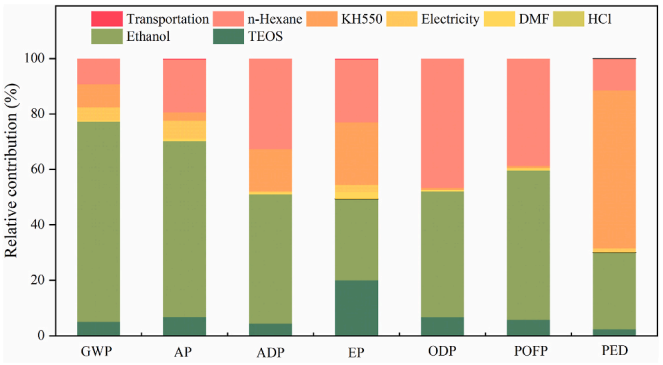

Fig. 14. Relative contribution of environmental impact indicators for MASA-2.

Compliance with ethical standards

The authors declare no conflict of interest. This article does not contain any studies with human participants and/or animals. Informed consent was obtained from all individual participants included in the study.

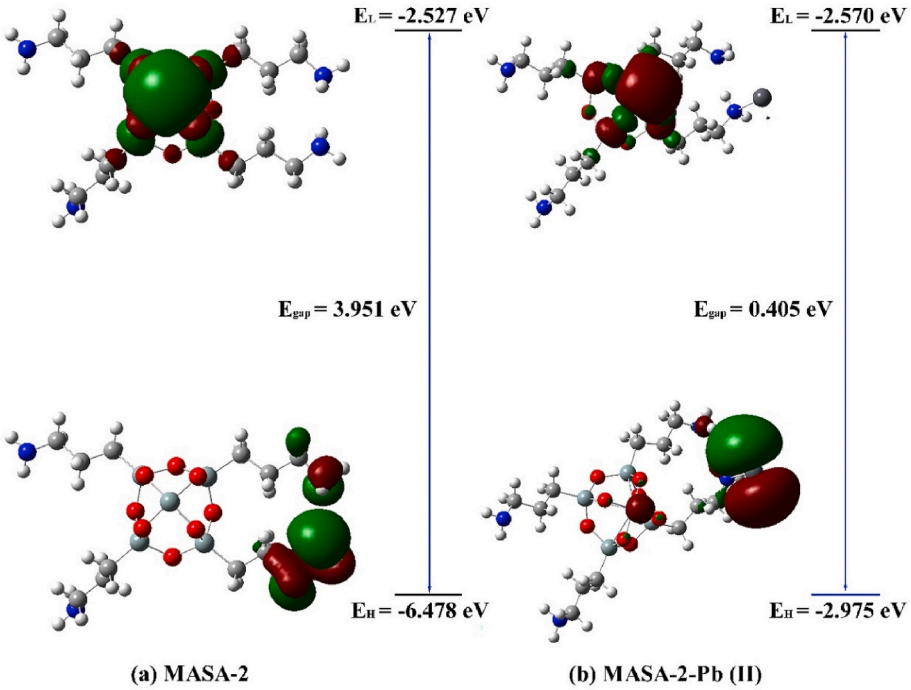

Fig. 13. HOMO and LUMO plots of (A) MASA-2, and (B) MASA-2-Pb (II).

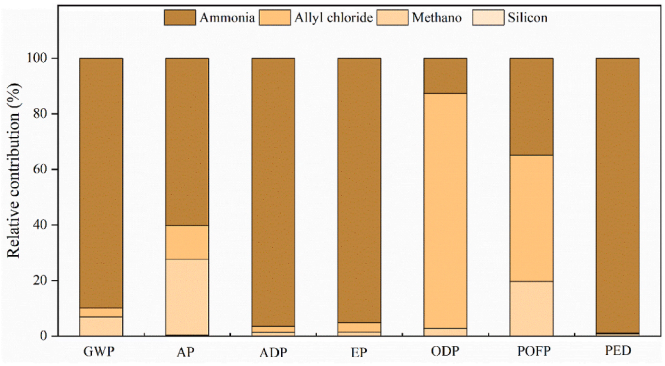

Fig. 15. Relative contribution of environmental impact indicators for KH550.

CRediT authorship contribution statement

Yaoyao Zhang: Writing – original draft, Software, Formal analysis. **Luca Magagnin:** Writing – review & editing, Supervision. **Kangze Yuan:** Writing – review & editing, Resources, Project administration, Funding acquisition, Conceptualization. **Zhengwen Wei:** Software. **Xishe Wu:** Resources, Methodology. **Zhenyi Jiang:** Software. **Wei Wang:** Writing – review & editing, Supervision.

Declaration of competing interest

The authors declare that they have no known competing financial interests or personal relationships that could have appeared to influence the work reported in this paper.

Data availability

Data will be made available on request.

Acknowledgments

This work was supported by the National Natural Science Foundation of China (51678059), the Key Research and Development Program of Shaanxi Province (2019GY-179), the Innovative Research Team for Science and Technology of Shaanxi Province (2022TD-04), the National Foreign Expert Project of China (G2021171031L), and the China Scholarship Council.

Appendix A. Supplementary data

Supplementary data to this article can be found online at https://doi.org/10.1016/j.micromeso.2022.112280.

References

[1] Y. Liu, J. Xu, Z. Cao, R. Fu, C. Zhou, Z. Wang, X. Xu, Adsorption behavior and mechanism of Pb (II) and complex Cu (II) species by biowaste-derived char with amino functionalization, J. Colloid Interface Sci. 559 (2020) 215–225, https://doi.org/10.1016/j.jcis.2019.10.035.

[2] L. Wang, J. Li, J. Wang, X. Guo, X. Wang, J. Choo, L. Chen, Green multi-functional monomer based ion imprinted polymers for selective removal of copper ions from aqueous solution, J. Colloid Interface Sci. 541 (2019) 376–386, https://doi.org/10.1016/j.jcis.2019.01.081.

[3] F. Wu, L. Chen, P. Hu, Y. Wang, J. Deng, B. Mi, Industrial alkali lignin-derived biochar as highly efficient and low-cost adsorption material for Pb (II) from aquatic environment, Bioresour. Technol. 322 (2021), 124539, https://doi.org/10.1016/j.biortech.2020.124539.

[4] Q. Chen, Y. Yao, X. Li, J. Lu, J. Zhou, Z. Huang, Comparison of heavy metal removals from aqueous solutions by chemical precipitation and characteristics of precipitates, J. Water Proc. Eng. 26 (2018) 289–300, https://doi.org/10.1016/j.jwpe.2018.11.003.

[5] J.P. Bezzina, L.R. Ruder, R. Dawson, M.D. Ogden, Ion exchange removal of Cu (II), Fe (II), Pb (II) and Zn (II) from acid extracted sewage sludge-Resin screening in weak acid media, Water Res. 158 (2019) 257–267, https://doi.org/10.1016/j.watres.2019.04.042.

[6] S. Jamshidifarda, S. Koushkbaghib, S. Hosseini, S. Rezaei, A. Karamipour, A.J. Rad, M. Irani, Incorporation of UiO-66-NH_2 MOF into the PAN/chitosan nanofibers for adsorption and membrane filtration of Pb (II), Cd (II) and Cr (VI) ions from aqueous solutions, J. Hazard Mater. 368 (2019) 10–20, https://doi.org/10.1016/j.jhazmat.2019.01.024.

[7] R. Pelalak, Z. Heidari, S.M. Khatami, T.A. Kurniawan, A. Marjani, S. Shirazian, Oak wood ash/GO/Fe_3O_4 adsorption efficiencies for cadmium and lead removal from aqueous solution: kinetics, equilibrium and thermodynamic evaluation, Arab. J. Chem. 14 (2021), 102991, https://doi.org/10.1016/j.arabjc.2021.102991.

[8] X. Li, H. Li, X. Xu, N. Guo, L. Yuan, H. Yu, Preparation of a reduced graphene oxide @ stainless steel net electrode and its application of electrochemical removal Pb (II), J. Electrochem. Soc. 164 (2017) E71–E77, https://doi.org/10.1149/2.1211704jes.

[9] N.B. Singh, G. Nagpal, S. Agrawal, Rachna, water purification by using adsorbents: a review, Environ. Technol. Innovat. 11 (2018) 187–240, https://doi.org/10.1016/j.eti.2018.05.006.

[10] Y. Wu, H. Pang, Y. Liu, X. Wang, S. Yu, D. Fu, J. Chen, X. Wang, Environmental remediation of heavy metal ions by novel-nanomaterials: a review, Environ. Pollut. 246 (2019) 608–620, https://doi.org/10.1016/j.envpol.2018.12.076.

[11] Z. Zhang, T. Wang, H. Zhang, Y. Liu, B. Xing, Adsorption of Pb (II) and Cd (II) by magnetic activated carbon and its mechanism, Sci. Total Environ. 757 (2021), 143910, https://doi.org/10.1016/j.scitotenv.2020.143910.

[12] G. Li, B. Wang, Q. Sun, W.Q. Xu, Y. Han, Adsorption of lead ion on amino-functionalized fly-ash-based SBA-15 mesoporous molecular sieves prepared via two-step hydrothermal method, Microporous Mesoporous Mater. 252 (2017) 105–115, https://doi.org/10.1016/j.micromeso.2017.06.004.

[13] S. Gu, X. Kang, L. Wang, E. Lichtfouse, C. Wang, Clay mineral adsorbents for heavy metal removal from wastewater: a review, Environ. Chem. Lett. 17 (2019) 629–654, https://doi.org/10.1007/s10311-018-0813-9.

[14] S.S. Fiyadh, M.A. AlSaadi, W.Z. Jaafar, M.K. AlOmar, S.S. Fayaed, N.S. Mohd, L. S. Hin, A. El-Shafie, Review on heavy metal adsorption processes by carbon nanotubes, J. Clean. Prod. 230 (2019) 783–793, https://doi.org/10.1016/j.jclepro.2019.05.154.

[15] D.C. da Silva Alves, B. Healy, L.A. Pinto, T.R. Cadaval, C.B. Breslin, Recent developments in chitosan-based adsorbents for the removal of pollutants from aqueous environments, Molecules 26 (2021) 594, https://doi.org/10.3390/molecules26030594.

[16] Y. Li, C. Guo, R. Shi, H. Zhang, L. Gong, L. Dai, Chitosan/nanofibrillated cellulose aerogel with highly oriented microchannel structure for rapid removal of Pb (II) ions from aqueous solution, Carbohydr. Polym. 223 (2019), 115048, https://doi.org/10.1016/j.carbpol.2019.115048.

[17] Y. Zhang, M. Xia, F. Wang, Ji Ma, Experimental and theoretical study on the adsorption mechanism of Amino trimethylphosphate (ATMP) functionalized hydroxyapatite on Pb (II) and Cd (II), Colloids Surf. A Physicochem. Eng. Asp. 626 (2021), 127029, https://doi.org/10.1016/j.colsurfa.2021.127029.

[18] P.O. Oladoye, Natural, low-cost adsorbents for toxic Pb (II) ion sequestration from (waste)water: a state-of-the-art review, Chemosphere 287 (2022), 132130, https://doi.org/10.1016/j.chemosphere.2021.132130.

[19] L. Han, T. Wang, J. Gon, X. Li, Y. Ji, S. Wang, Multi-hydroxyl containing organo-vermiculites for enhanced adsorption of coexisting methyl blue and Pb (II) and their adsorption mechanisms, Colloids Surf. A Physicochem. Eng. Asp. 650 (2022), 129542, https://doi.org/10.1016/j.colsurfa.2022.129542.

[20] J.P. Vareda, A.J. Valente, L. Durães, Heavy metals in Iberian soils: removal by current adsorbents/amendments and prospective for aerogels, Adv. Colloid Interface Sci. 237 (2016) 28–42, https://doi.org/10.1016/j.cis.2016.08.009.

[21] S.S. Çok, F. Koç, N. Gizli, Lightweight and highly hydrophobic silica aerogels dried in ambient pressure for an efficient oil/organic solvent adsorption, J. Hazard Mater. 408 (2021), 124858, https://doi.org/10.1016/j.jhazmat.2020.124858.

[22] T. Liu, Q. Liu, Y. Liu, H. Yao, Z. Zhang, X. Wang, J. Shen, Fabrication of methyl acrylate modified silica aerogel for capture of Cu^{2+} from aqueous solutions, J. Sol. Gel Sci. Technol. 98 (2021) 389–400, https://doi.org/10.1007/s10971-021-05499-w.

[23] N.V. Stolyarchuk, V.V. Tomina, B. Mishra, B.P. Tripathi, M. Vaclavikova, O. A. Dudarko, I.V. Melnyk, Direct synthesis of efficient silica-based adsorbents carrying EDTA groups for the separation of Cu (II) and Ni (II) ions, Colloids Surf. A Physicochem. Eng. Asp. (2022), 129538, https://doi.org/10.1016/j.colsurfa.2022.129538.

[24] L. Durães, H. Maleki, J.P. Vareda, A. Lamy-Mendes, A. Portugal, Exploring the versatile surface chemistry of silica aerogels for multipurpose application, MRS Adv 375 (2017) 3511–3519, https://doi.org/10.1557/adv.2017.375.

[25] R. Wang, Y. Li, X. Shuai, J. Chen, R. Liang, C. Liu, Development of pectin-based aerogels with several excellent properties for the adsorption of Pb^{2+}, Foods 10 (2021) 3127, https://doi.org/10.3390/foods10123127.

[26] A. Lamy-Mendes, R.B. Torres, J.P. Vareda, D. Lopes, M. Ferreira, V. Valente, A. V. Girão, A.J.M. Valente, L. Durães, Amine modification of silica aerogels/xerogels for removal of relevant environmental pollutants, Molecules 24 (2019) 3701, https://doi.org/10.3390/molecules24203701.

[27] A.F. Abdel-Magied, H.N. Abdelhamid, R.M. Ashour, L. Fu, M. Dowaidar, W. Xia, K. Forsberg, Magnetic metal-organic frameworks for efficient removal of cadmium (II), and lead(II) from aqueous solution, J. Environ. Chem. Eng. 10 (2022), 107467, https://doi.org/10.1016/j.jece.2022.107467.

[28] C.-Z. Zhang, Y. Yuan, Z. Guo, Experimental study on functional graphene oxide containing many primary amino groups fast-adsorbing heavy metal ions and

adsorption mechanism, Separ. Sci. Technol. 53 (2018) 1666–1677, https://doi.org/10.1080/01496395.2018.1436071.
[29] F. Zhu, L. Li, J. Xing, Selective adsorption behavior of Cd(II) ion imprinted polymers synthesized by microwave-assisted inverse emulsion polymerization: adsorption performance and mechanism, J. Hazard Mater. 321 (2017) 103–110, https://doi.org/10.1016/j.jhazmat.2016.09.012.
[30] B. Cao, J. Qu, Y. Yuan, W. Zhang, X. Miao, X. Zhang, Y. Xu, T. Han, H. Song, S. Ma, X. Tian, Y. Zhang, Efficient scavenging of aqueous Pb(II)/Cd(II) by sulfide-iron decorated biochar: performance, mechanisms and reusability exploration, J. Environ. Chem. Eng. 10 (2022), 107531, https://doi.org/10.1016/j.jece.2022.107531.
[31] L. Zhao, K. Shen, B. Li, Y. Zhang, S. Zhang, Y. Hong, J. Zhang, Z. Li, Exploration of novel high-temperature heavy metals adsorbent for sludge incineration process: experiments and theoretical calculations, J. Environ. Chem. Eng. 10 (2022), 107755, https://doi.org/10.1016/j.jece.2022.107755.
[32] ILCD (International Reference Life Cycle Data System), General Guide for Life Cycle Assessment (LCA)-detailed Guidance, Ispra,Italy: Joint Research Centre, Institute for Environment and Sustainability, 2010.
[33] V.K. Gupta, Suhas, Application of low-cost adsorbents for dye removal - a review, J. Environ. Manag. 90 (2009) 2313–2342, https://doi.org/10.1016/j.jenvman.2008.11.017.
[34] M. Frisch, G. Trucks, H.B. Schlegel, G.E. Scuseria, M.A. Robb, J.R. Cheeseman, G. Scalmani, V. Barone, B. Mennucci, G. Petersson, Gaussian 09, Revision d.01, Gaussian, Wallingford CT, 2009, p. 201.
[35] L. Sellaoui, D.I. Mendoza-Castillo, H.E. Reynel-Ávila, B.A. Ávila-Camacho, L. L. Díaz-Muñoz, H. Ghalla, A. Bonilla-Petriciolet, A.B. Lamine, Understanding the adsorption of Pb^{2+}, Hg^{2+} and Zn^{2+} from aqueous solution on a lignocellulosic biomass char using advanced statistical physics models and density functional theory simulations, Chem. Eng. J. 365 (2019) 305–316, https://doi.org/10.1016/j.cej.2019.02.052.
[36] C. Ji, M. Xu, H. Yu, L. Lv, W. Zhang, Mechanistic insight into selective adsorption and easy regeneration of carboxyl-functionalized MOFs towards heavy metals, J. Hazard Mater. 424 (2022), 127684, https://doi.org/10.1016/j.jhazmat.2021.127684.
[37] B. Wang, J. Xuan, X. Yang, Z. Bai, Synergistic DFT-guided design and microfluidic synthesis of high-performance ion-imprinted biosorbents for selective heavy metal removal, Colloids Surf. A Physicochem. Eng. Asp. 626 (2021), 127030, https://doi.org/10.1016/j.colsurfa.2021.127030.
[38] L. Wang, W.H. Xu, R. Yang, T. Zhou, D. Hou, X. Zheng, J.H. Liu, X.J. Huang, Electrochemical and density functional theory investigation on high selectivity and sensitivity of exfoliated nano-zirconium phosphate toward lead(II), Anal. Chem. 85 (2013) 3984–3990, https://doi.org/10.1021/ac3037014.
[39] K. Chen, Q. Feng, Y. Feng, D. Ma, D. Wang, Z. Liu, W. Zhu, X. Li, F. Qin, J. Feng, Ultrafast removal of humic acid by amine-modified silica aerogel: insights from experiments and density functional theory calculation, Chem. Eng. J. 435 (2022), 135171, https://doi.org/10.1016/j.cej.2022.135171.
[40] L. Xu, Y. Liu, J. Wang, Y. Tang, Z. Zhang, Selective adsorption of Pb^{2+} and Cu^{2+} on amino-modified attapulgite: kinetic, thermal dynamic and DFT studies, J. Hazard Mater. 404 (2021), 124140, https://doi.org/10.1016/j.jhazmat.2020.124140.
[41] ISO 14044, Environmental Management-Life Cycle Assessment-Requirements and Guidelines. Geneva, Switzerland, 2006.
[42] P.C. Ferrão, Industrial Ecology-Principles and Tools, 2009 (In Portuguese).
[43] Y. Guo, X.Q. Jiang, H.M. Wu, Y. Xiao, D.F. Wu, X. Liu, Preparation of 2-hydroxy-1-naphthalene functionalized SBA-15 adsorbent for the adsorption of chromium(III) ions from aqueous solution, J. Inorg. Mater. 36 (2021) 1163–1170, https://doi.org/10.15541/jim20210109.
[44] N. Yao, S. Cao, K.L. Yeung, Mesoporous TiO_2–SiO_2 aerogels with hierarchal pore structures, Microporous Mesoporous Mater. 117 (2009) 570–579, https://doi.org/10.1016/j.micromeso.2008.08.020.
[45] Z. Yu, X. Chen, Y. Zhang, H. Tu, P. Pan, S. Li, Y. Han, M. Piao, J. Hu, F. Shi, X. Yang, Phosphotungstic acid and propylsulfonic acid bifunctionalized ordered mesoporous silica: a highly efficient and reusable catalysts for esterification of oleic acid, Chem. Eng. J. 430 (2022), 133059, https://doi.org/10.1016/j.cej.2021.133059.
[46] K. Chen, Q. Feng, D. Ma, X. Huang, Hydroxyl modification of silica aerogel: an effective adsorbent for cationic and anionic dyes, Colloids Surf. A Physicochem. Eng. Asp. 616 (2021), 126331, https://doi.org/10.1016/j.colsurfa.2021.126331.
[47] Y. Zhang, Q. Shen, X. Li, H. Xie, C. Nie, Facile synthesis of ternary flexible silica aerogels with coarsened skeleton for oil-water separation, RSC Adv. 10 (2020) 42297–42304, https://doi.org/10.1039/D0RA07906E.
[48] N. Guerrero-Alburquerque, S. Zhao, N. Adilien, M.M. Koebel, M. Lattuada, W. J. Malfait, Strong, machinable, and insulating chitosan-urea aerogels: toward ambient pressure drying of biopolymer aerogel monoliths, ACS Appl. Mater. Interfaces 12 (2020) 22037–22049, https://doi.org/10.1021/acsami.0c03047.
[49] V. Hernández-Morales, R. Nava, Y.J. Acosta-Silva, S.A. Macías-Sánchez, J.J. Pérez-Bueno, B. Pawelec, Adsorption of lead (II) on SBA-15 mesoporous molecular sieve functionalized with -NH_2 groups, Microporous Mesoporous Mater. 160 (2012) 133–142.
[50] H.M. Wu, Y. Xiao, Y. Guo, S.J. Miao, Q.Q. Chen, Z. Chen, Functionalization of SBA-15 mesoporous materials with 2-acetylthiophene for adsorption of Cr(III) ions, Microporous Mesoporous Mater. 292 (2020), 109754, https://doi.org/10.1016/j.micromeso.2019.109754.
[51] S. Zhu, M.A. Khan, T. Kameda, H. Xu, F. Wang, M. Xia, T. Yoshioka, New insights into the capture performance and mechanism of hazardous metals Cr^{3+} and Cd^{2+} onto an effective layered double hydroxide based material, J. Hazard Mater. 426 (2022), 128062, https://doi.org/10.1016/j.jhazmat.2021.128062.
[52] D. Kundu, S.K. Mondal, T. Banerjee, Development of β-cyclodextrin-cellulose/hemicellulose-based hydrogels for the removal of Cd (II) and Ni (II): synthesis, kinetics, and adsorption aspects, J. Chem. Eng. Data 64 (2019) 2601–2617, https://doi.org/10.1021/acs.jced.9b00088.
[53] J. Maity, S.K. Ray, Competitive removal of Cu (II) and Cd (II) from water using a biocomposite hydrogel, J. Phys. Chem. B 121 (2017) 10988–11001, https://doi.org/10.1021/acs.jpcb.7b08796.
[54] Q. Fu, S. Zhou, P. Wu, J. Hu, J. Lou, B. Du, C. Mo, W. Yan, J. Luo, Regenerable zeolitic imidazolate frameworks@agarose (ZIF-8@AG) composite for highly efficient adsorption of Pb (II) from water, J. Solid State Chem. 307 (2022), 122823, https://doi.org/10.1016/j.jssc.2021.122823.
[55] T. Shahnaz, V. Sharma, S. Subbiah, S. Narayanasamy, Multivariate optimisation of Cr (VI), Co (III) and Cu (II) adsorption onto nanobentonite incorporated nanocellulose/chitosan aerogel using response surface methodology, J. Water Proc. Eng. 36 (2020), 101283, https://doi.org/10.1016/j.jwpe.2020.101283.
[56] Y. Gao, R.Y. Zhou, L. Yao, W. Yin, J.X. Yu, Q. Yue, Z. Xue, H. He, B. Gao, Synthesis of rice husk-based ion-imprinted polymer for selective capturing Cu (II) from aqueous solution and re-use of its waste material in Glaser coupling reaction, J. Hazard Mater. 424 (2022), 127203, https://doi.org/10.1016/j.jhazmat.2021.127203.
[57] H. Yang, M. Lu, D. Chen, R. Chen, L. Li, W. Han, Efficient and rapid removal of Pb^{2+} from water by magnetic Fe_3O_4@MnO_2 core-shell nanoflower attached to carbon microtube: adsorption behavior and process study, J. Colloid Interface Sci. 563 (2020) 218–228, https://doi.org/10.1016/j.jcis.2019.12.065.
[58] Z. Feng, N. Chen, T. Liu, C. Feng, $KHCO_3$ activated biochar supporting MgO for Pb (II) and Cd (II) adsorption from water: experimental study and DFT calculation analysis, J. Hazard Mater. 426 (2022), 128059, https://doi.org/10.1016/j.jhazmat.2021.128059.
[59] H. Sun, Z. Ji, Y. He, L. Wang, J. Zhan, L. Chen, Y. Zhao, Preparation of PAMAM modified PVDF membrane and its adsorption performance for copper ions, Environ. Res. 204 (2022), 111943, https://doi.org/10.1016/j.envres.2021.111943.
[60] S. Yadav, A. Asthana, A.K. Singh, R. Chakraborty, S.S. Vidya, M. Susan, S.A. C. Carabineiro, Adsorption of cationic dyes, drugs and metal from aqueous solutions using a polymer composite of magnetic/beta-cyclodextrin/activated charcoal/Na alginate: isotherm, kinetics and regeneration studies, J. Hazard Mater. 409 (2021), 124840, https://doi.org/10.1016/j.jhazmat.2020.124840.
[61] A.A. Alqadami, M. Naushad, Z.A. ALOthman, M. Alsuhybani, M. Algamdi, Excellent adsorptive performance of a new nanocomposite for removal of toxic Pb (II) from aqueous environment: adsorption mechanism and modeling analysis, J. Hazard Mater. 389 (2020), 121896, https://doi.org/10.1016/j.jhazmat.2019.121896.
[62] T. Tatarchuk, M. Myslin, I. Mironyuk, M. Bououdina, A.T. Pędziwiatr, R. Gargula, B.F. Bogacz, P. Kurzydło, Synthesis, morphology, crystallite size and adsorption properties of nanostructured Mg-Zn ferrites with enhanced porous structure, J. Alloys Compd. 819 (2020), 152945, https://doi.org/10.1016/j.jallcom.2019.152945.
[63] Y. Guo, D.F. Wu, H.M. Wu, X.Y. Liu, H.Z. Xu, Q.Q. Chen, Efficient removal of Pb(II) ions by using 2-acetylthiophene-modified graphene oxide from aqueous solution, Materials Today Sustainability 20 (2022), 100212, https://doi.org/10.1016/j.mtsust.2022.100212.
[64] E.C. Nnadozie, P.A. Ajibade, Adsorption, kinetic and mechanistic studies of Pb(II) and Cr(VI) ions using APTES functionalized magnetic biochar, Microporous Mesoporous Mater. 309 (2020), 110573, https://doi.org/10.1016/j.micromeso.2020.110573.
[65] Y. Guo, Y. Xiao, H.M. Wu, J.W. Xu, Q.Q. Chen, Efficient removal of Pb(II) ions from aqueous solution by using a novel functionalized bio-material with two tridentate coordinated units, J. Chem. Technol. Biotechnol. 96 (2021) 1709–1719, https://doi.org/10.1002/jctb.6696.
[66] Z.C. Ji, H.Y. Sun, Y.F. Zhu, D.D. Zhang, L.H. Wang, F.Y. Dai, Y.P. Zhao, L. Chen, Enhanced selective removal of lead ions using a functionalized PAMAM@UiO-66-NH_2 nanocomposite: experiment and mechanism, Microporous Mesoporous Mater. 328 (2021), 111433, https://doi.org/10.1016/j.micromeso.2021.111433.
[67] X.T. Yang, G.P. Zhu, Y.X. Liu, Q.Y. Wang, N. Gu, Y. Zeng, X.R. Han, D.B. Yu, H. W. Yu, Enhanced removal of Pb(II) from contaminated water by hierarchical titanate microtube derived from titanium glycolate, Adv. Powder Technol. 33 (2022), 103376, https://doi.org/10.1016/j.apt.2021.11.028.
[68] D.D. Liu, Z.K. Hao, D.Q. Chen, L.P. Jiang, T.Q. Li, Y. Luo, C.P. Yan, B. Tian, B.Y. Jia, G. Chen, Hierarchical porous biochar fabricated by *Aspergillus tubingensis* pretreatment coupling with chemical activation for Pb (II) removal, Microporous Mesoporous Mater. 335 (2022), 111861, https://doi.org/10.1016/j.micromeso.2022.111861.
[69] R. Chakraborty, R. Verma, A. Asthana, S.S. Vidya, A.K. Singh, Adsorption of hazardous chromium (VI) ions from aqueous solutions using modified sawdust: kinetics, isotherm and thermodynamic modelling, Int. J. Environ. Anal. Chem. 101 (2019) 911–928, https://doi.org/10.1080/03067319.2019.1673743.
[70] K. Dai, G. Liu, W. Xu, Z. Deng, Y. Wu, C. Zhao, Z. Zhang, Judicious fabrication of bifunctionalized graphene oxide/$MnFe_2O_4$ magnetic nanohybrids for enhanced removal of Pb (II) from water, J. Colloid Interface Sci. 579 (2020) 815–822, https://doi.org/10.1016/j.jcis.2020.06.085.
[71] C. Ji, Y. Ren, H. Yu, M. Hua, L. Lv, W. Zhang, Highly efficient and selective Hg (II) removal from water by thiol-functionalized MOF-808: kinetic and mechanism study, Chem. Eng. J. 430 (2022), 132960, https://doi.org/10.1016/j.cej.2021.132960.
[72] S.F. Lütke, A.V. Igansi, L. Pegoraro, G.L. Dotto, L.A.A. Pinto, T.R.S. Cadaval, Preparation of activated carbon from black wattle bark waste and its application

for phenol adsorption, J. Environ. Chem. Eng. 7 (2019), 103396, https://doi.org/10.1016/j.jece.2019.103396.
[73] R. Fu, Y. Liu, Z. Lou, Z. Wang, S.A. Baig, X. Xu, Adsorptive removal of Pb (II) by magnetic activated carbon incorporated with amino groups from aqueous solutions, J. Taiwan Inst. Chem. Eng. 62 (2016) 247–258, https://doi.org/10.1016/j.jtice.2016.02.012.
[74] L. Hou, G. Qin, Y. Qu, C. Yang, X. Rao, Y. Gao, X. Zhu, Fabrication of recoverable magnetic composite material based on graphene oxide for fast removal of lead and cadmium ions from aqueous solution, J. Chem. Technol. Biotechnol. 96 (2021) 1345–1357, https://doi.org/10.1002/jctb.6655.
[75] J. Zhao, C. Wang, S. Wang, Y. Zhou, Experimental and DFT study of selective adsorption mechanisms of Pb(II) by UiO-66-NH_2 modified with 1,8-dihydroxyanthraquinone, J. Ind. Eng. Chem. 83 (2020) 111–122, https://doi.org/10.1016/j.jiec.2019.11.019.
[76] M. Rezaei-Sameti, P. Zarei, A.I.M. NBO, HOMO-LUMO and thermodynamic investigation of the nitrate ion adsorption on the surface of pristine, Al and Ga doped BNNTs: a DFT study, Adsorption 24 (2018) 757–767, https://doi.org/10.1007/s10450-018-9977-7.
[77] J. Zhang, T. Li, X. Li, Y. Liu, N. Li, Y. Wang, X. Li, A key role of inner-cation-pi interaction in adsorption of Pb(II) on carbon nanotubes: experimental and DFT studies, J. Hazard Mater. 412 (2021), 125187, https://doi.org/10.1016/j.jhazmat.2021.125187.
[78] Y. Guo, H. Wang, L. Zeng, SiO_2 aerogels prepared by ambient pressure drying with ternary azeotropes as components of pore fluid, J. Non-Cryst. Solids 428 (2015) 1–5, https://doi.org/10.1016/j.jnoncrysol.2015.07.030.
[79] S. Motahari, M. Nodeh, K. Maghsoudi, Absorption of heavy metals using resorcinol formaldehyde aerogel modified with amine groups, Desalination Water Treat. 57 (2016) 16886–16897, https://doi.org/10.1080/19443994.2015.1082506.
[80] W. Zhan, L. Gao, X. Fu, S.H. Siyal, G. Sui, X. Yang, Green synthesis of amino-functionalized carbon nanotube-graphene hybrid aerogels for high performance heavy metal ions removal, Appl. Surf. Sci. 467–468 (2019) 1122–1133, https://doi.org/10.1016/j.apsusc.2018.10.248.
[81] S. Anselmo, S. Cataldo, T. Avola, G. Sancataldo, M.C. D'Oca, T. Fiore, N. Muratore, M. Scopelliti, A. Pettignano, V. Vetri, Lead (II) ions adsorption onto amyloid particulates: an in depth study, J. Colloid Interface Sci. 610 (2022) 347–358, https://doi.org/10.1016/j.jcis.2021.11.184.